Plasma-Induced Erosion on Ceramic Wall Structures in Hall-Effect Thrusters

Thomas Burton*
University of Alabama, Tuscaloosa, Alabama 35487

Aaron M. Schinder,† German Capuano,† Julian J. Rimoli,† and Mitchell L. R. Walker†
Georgia Institute of Technology, Atlanta, Georgia 30332
and
Gregory B. Thompson‡
University of Alabama, Tuscaloosa, Alabama 35487

A 60 wt% boron nitride (BN)–40 wt% silica (SiO₂) hot-pressed composite, denoted as M26, was used as the insulating chamber wall for a xenon plasma Hall-effect thruster operated for approximately 2000 h at power levels between 1.5 and 5 kW. The chamber wall showed a range of erosion microstructures. In the heavily eroded regions, striations in the surface topology were evident with surface protrusions in the generic shape of conical tips consisting of stratified BN and silica phases. Microcracking along the long axis of the BN basal plane was prevalent. Through a two-dimensional finite element model, the microcracking has been determined to occur because of the anisotropic thermal expansion of BN in the amorphous silica matrix. Exfoliation accompanied the microcracking in BN and resulted in the preferential loss of BN as compared with silica in these heavily eroded regions.

Introduction

HALL-effect thrusters (HETs) are attractive candidates for geosynchronous station keeping and similar low-thrust space-based propulsion applications [1,2]. They are capable of much greater ion current density than gridded ion thrusters because of the quasi neutrality of the plasma used as the propulsion source [3]. They also operate in a lower specific impulse regime of approximately 1500 s at constant power, which yields a greater thrust-to-power ratio [4]. Recent qualification life testing of the Aerojet 4.5 kW BPT-4000 HET has shown that HETs can achieve operational lifetimes comparable to the lifespan of ion engines such as the NASA NSTAR engine [5,6].

One of the limiting factors for HET service life and propulsion performance is the ability of the chamber wall to withstand plasma-driven erosion in the discharge channels [4,6–8]. With the erosion of the chamber walls, the surface topology is altered. The formation of ledges, kinks, and other similar microstructural features are sites that can concentrate electric fields, thereby locally influencing the secondary electron emission [9]; consequently, the plasma equilibrium boundary conditions change [4,8]. Additionally, Gascon et al. [7] noted that the discharge current is a function of material type. If the wall is a composite microstructure, with each phase eroding at a different rate, the relative surface emission behavior will vary depending on the surface composition as well as the surface morphology. Moreover, after the walls are fully eroded, the plasma itself can affect the magnetic field geometry by sputtering the magnetic material that was previously behind the protective wall material. Understanding the erosion mechanisms and their effect on the microstructure of the chamber wall will shed light on the physical processes that govern erosion. Based on the erosion features of the BPT-4000, observed during its 10,400 h life test, it is clear that current erosion models do not capture the physics of the lifetime limiting mechanisms. Recent research by the Jet

Propulsion Laboratory has shown that there may be alternatives to avoiding these erosion mechanisms [10].

There have been several studies on ion-based erosion in ceramic materials [5–8,10–17]. The mechanisms of erosion include sputtering by the plasma ions bombarding the surface, thermal stresses, and ion implantations into the substrate. These processes can initiate crack failures in the materials from localized strain from implanted species and possibly weaken intergranular bonding by the segregation of these implanted ions diffusing to the grain boundaries. Specific to HETs, a detailed microstructural characterization of the surface can reveal the dominate mechanisms of erosion that lead to failure. By identifying these features, means to engineer the material for improved sustainability or performance can then be developed [18]. To date, quasi-empirical models are used to predict HET service lifetimes and performance [11,13–15] with little information on the dominating mechanisms that contribute to erosion. Some features of the erosion that are not reproduced by present models include the microstructure-driven surface features that are produced during erosion, variation in the composition of the surface [15,19], and large length scale features such as the anomalous saw tooth erosion ridges seen during the BPT-4000 qualification life test. [5]

The U.S. Air Force Research Laboratory/University of Michigan P5 HET uses a boron nitride (BN)–silica (SiO₂) composite designated as grade M (40% BN, 60% SiO₂ by weight) or M26 (60% BN, 40% SiO₂ by weight) material for the chamber wall [20]. This composite material has a good combination of machinability for fabrication, secondary electron emission for HET operation, and ion erosion characteristic properties that enable sufficient HET lifetime [21]. In particular, the high secondary electron emission is desirable to help to reduce the electron temperature in a stationary plasma thruster [20]. The reduction in electron temperature has been shown to increase HET efficiency [7]. A consequence of a heterogeneous phase composite is that each phase has a different sputtering yield, thermal expansion, and mechanical properties. These differences could contribute to nonuniform microstructural instabilities resulting from preferential erosion. This paper aims at quantifying how the composite phases within such a microstructure evolve along different regions within the HET chamber wall.

*Department of Metallurgical and Materials Engineering.
†School of Aerospace Engineering.
‡Department of Metallurgical and Materials Engineering; gthompson@eng.ua.edu (Corresponding Author).

Experimental Setup

A M26 grade Combat© 60 wt % boron nitride (BN)–40 wt% silica (SiO₂) hot-pressed composite, manufactured by Saint Gobain

Ceramic Materials Company, was used as the thruster channel wall material in the HET. The M26 material was part of a P5 HET operated for approximately 2000 h at power levels between 1.5 and 5 kW in xenon plasma. Please consult [22] for details on the service performance of the thruster. After plasma operation, a piece of the annular M26 wall's channel ring was mechanically removed, sectioned, and mounted onto appropriate fixture for microstructural characterization, as shown in Fig. 1.

The phase identification of the subsectioned ring was determined by x-ray diffraction (XRD) using a Bruker Discovery D8 diffractometer operated with cobalt k_α radiation at 45 keV and 20 mA. Scanning electron microscopy (SEM) imaging of the surface was performed using a JEOL 7000F operated at 10 keV. Because the composite material is known to have low electrical conductivity [23], the samples were either gold coated or carbon coated to reduce surface charging, which leads to image degradation. Most of the micrographs were images of the direct, eroded surface; when polishing was required, the sample was automechanically polished using 9 and 3 μm diamond suspensions with a final vibromet polish with a 0.05 μm silica slurry suspension. The chemical signature from the surface was quantified by x-ray photoelectron spectroscopy (XPS) in a Kratos Axis 165 operating at 12 KeV and 12 mA with a monochrome Al source, scanning from 0 to 1000 eV binding energy. Transmission electron microscopy (TEM) was done in a FEI Tecnai F20 Supertwin (Scanning) TEM operated at 200 keV. The (S)TEM foils were prepared by a focus ion beam in situ liftout procedure, the details of which can be found in [24]. Particular care was taken in the final focused ion beam milling steps to reduce potential Ga$^+$ ion implantation artifacts through low kiloelectron volt ion polishing [25].

Results

The sectioned M26 thruster revealed three distinct regions relative to their position in the HET. These have been designated as 1) low-erosion (LE), 2) moderate-erosion (ME), and 3) high-erosion (HE) regions, shown in Fig. 1. The distinction of these regions was determined by the discoloration, shown in Fig. 1b, and eroded microstructures, Figs. 1c–1e. The dark discoloration on the chamber wall, Fig. 1b, is caused by carbon redeposition from the downstream graphite beam dump in the vacuum facility. XRD in Fig. 2 revealed amorphous silica, evident by the broad hump between 20 and 30 deg

2Θ, and the narrow, intense crystalline peaks identified as the crystalline hexagonal close-packed (hcp) BN phase (hBN). No crystallographic phase transformations for the BN or silica phases were noted between each of the three erosion regions.

The SEM micrographs of Figs. 1c–1e revealed a significantly altered surface structure between the LE, ME, and HE regions, as previously reported by Pellerin et al. [11]. The LE region, Fig. 1e, revealed a granular microstructure commonly observed in hot-pressed powder mixtures. The ME region, Fig. 1d, revealed a polished-like surface appearance with striations of the grains and microcracking within the material. The HE region revealed three distinct surface features, shown in the magnified image in Fig. 3a. There were regions where it appeared that the BN phase exfoliated or flaked off from the matrix, leaving a smooth silica surface (denoted as "i" in Fig. 3a and magnified in Fig. 3b). In other regions, the surface was modified into jagged, surface protrusions (denoted as "ii" in Fig. 3a). These striated and jagged surface protrusions consisted of a stratified morphology of BN and silica evident from the contrast in the SEM backscattered image of Fig. 3c. As previously observed in the ME region, microcracking, denoted as "iii" in Fig. 3a, was also evident in the HE region. The backscattered SEM micrograph, Fig. 3d, of a polished surface from within the HE region revealed that the microcracks were predominantly in the BN phases with some smaller cracks in the silica matrix.

The inset electron diffraction patterns in Fig. 4 confirmed the crystalline hcp phase of BN and the amorphous structure of the silica. Similar to the backscattered SEM images, the high-angle annular dark field micrograph of Fig. 4 provides semiquantitative atomic phase imaging with brighter contrast indicative of the higher atomic number containing species [26]. This micrograph reveals that the microcracks are prevalent in the BN phase, with splitting widths that are a few nanometers and several cracks present in the same fiber. These cracks did not appear to bifurcate but ran parallel along the basal plane of BN, as determined by the edge-on zone axis of [02–20] diffraction pattern in the inset image of Fig. 4.

XPS revealed a relative compositional change, shown in the histogram of Fig. 5, between each of the elements in the three eroded regions. The relative carbon content increased into the HE region which attributed to the discoloration on the sample shown in Fig. 1b. As the wall material became more eroded, an increase in the relative
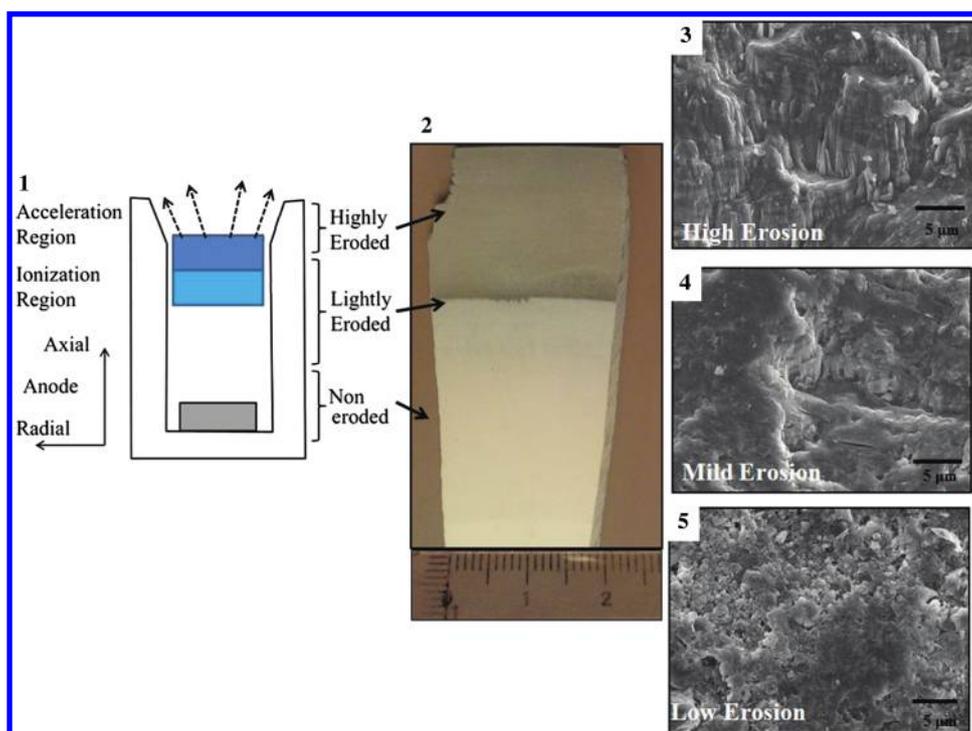

Fig. 1 a) Schematic of the HET thruster. b) Optical image of subsectioned HET wall with scale in inches. SEM micrographs of the c) highly eroded region, d) moderately eroded region, and e) low or noneroded region.
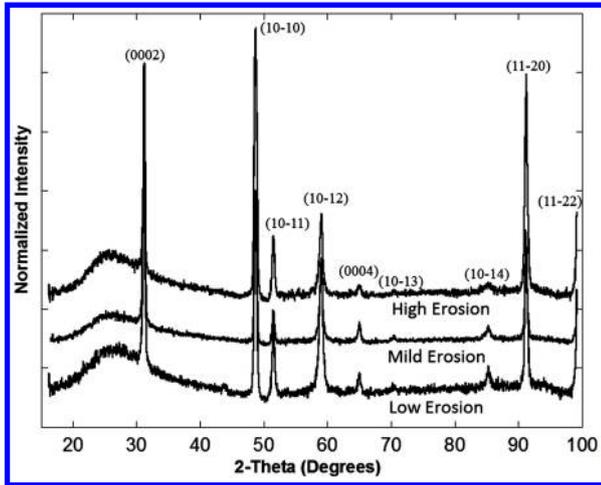
Fig. 2 XRD patterns from the three erosion regions.

Fig. 4 Scanning TEM micrograph from the moderate erosion region.

amounts of silicon and oxygen signals and a corresponding decrease in the boron and nitrogen signals were noted.

Discussion

After 2000 operational hours, specific regions of the chamber wall surface topology showed evidence of significant variation in erosion characteristics. The variation in erosion characteristics along the axial direction of the discharge chamber material is attributed to the spatial variation in the energy of ions that impact the discharge chamber wall. Between the anode exit plane and the ionization region, Fig. 1a, the HE portion of the wall is exposed to neutral gas temperatures of approximately 850 to 1000 K [27]. Once the plasma ionizes and accelerates across this region, a sharp potential drop near the exit plane of the thruster occurs and the ion impact energies of the ions, within the plasma, rise from <10 eV to between 100 and 300 eV. In addition to the plasma potential profile in the axial direction, the
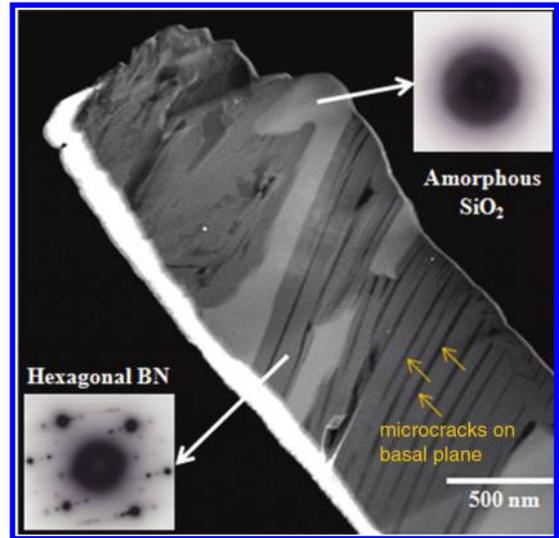
electron temperature peak near the exit plane also causes large sheath potentials, which can drive large additional changes in bombarding ion energy [28]. The increase in impact energy in this region is distinct and has a marked impact on the surface topology evident in the upstream chamber wall's microstructure shown between the micrographs in Figs. 1c–1e.

The preferential retention of silica as compared with BN in the highly eroded region, Fig. 5, roughens the surface topology by the variation in removal rates between the two phases. With longer exposures, this roughening is enhanced because the modulated surface topology would cause shadowing effects for line-of-sight ion implantation [29]. This would facilitate surface striations as seen the eroded microstructures [6]. In addition, the difference in sputtering rate between the two materials would cause shaping of the features. This is evident in the needle-like surface protrusions that formed.
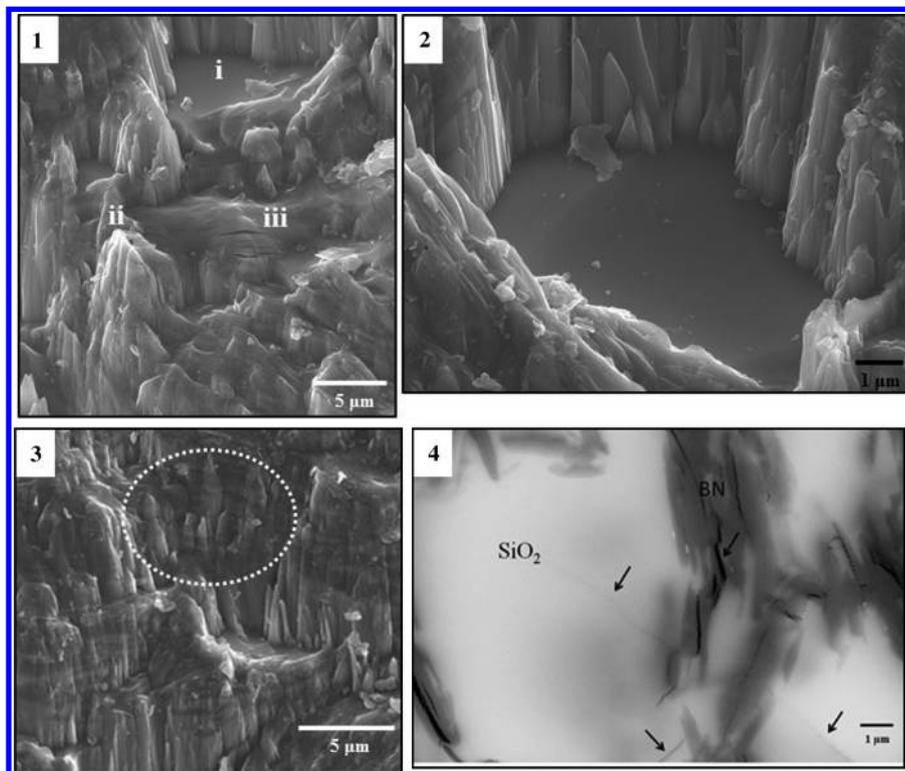

Fig. 3 a) SEM micrograph highlighting: i, a planar silica surface; ii, surface protrusions; and iii, microcracking. b) High-magnification micrograph of the planar silica surface. c) Backscattered SEM micrograph of the stratified morphology. d) Polished surface revealing significant microcracking; arrows point to cracks in silica.
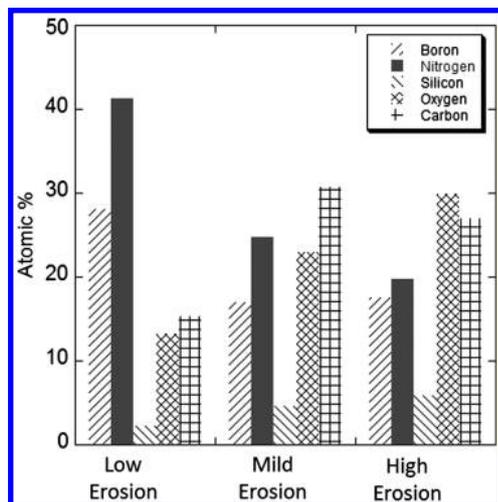
Fig. 5 XPS data of each constituent element from each of the three regions.

Upon closer evaluations, the backscattered SEM micrograph of Fig. 3c revealed a stratified silica–BN structure within these protrusions. The combined effects of line-of-site impingement and subsequent sputtering behavior intrinsic to each phase contributed to the surface protrusion development.

The retention of silica, evident by the XPS measurement, is surprising considering that silica's binding energy is approximately one-half that of BN [30], which could be expected to be more resistant to sputtering. The relative change in matrix phase composition observed in this work is in agreement with the previous report by Garnier et al. [15,16] and Pellerin et al. [11], but is in contradiction to Zidar and Rovey [19], who reported the retention of BN. Upon closer inspection of the backscattered images in the HE region, some sections appear to have a smooth silica surface. The prevalent microcracking in the BN is suggestive of structural instability within this phase caused by mechanical stress around the grain. Consequently, the smooth features represent regions where the BN fibers exfoliated from the matrix and are no longer contained in the material. The detachment of the BN phase leaves the remnant interphase boundary between the silica and BN exposed. This suggests that the interface bonding between the species is structurally insufficient to withstand the plasma eroding environment. The lack of significant roughening on this planar region is indicative that, either 1) the detachment occurred after the plasma was turned off and the ions did not impact the surface to roughen it, and/or 2) the surrounding, higher surface features provided shielding from the majority of line-of-site ion bombardment from the plasma. For the former, the thermal cycling of the chamber walls between operational and nonoperational periods would result in thermal expansion and contraction differences between the phases, which could lead to detachment of certain surface phases, as will be discussed next.

The presence of the microcracks within the BN fiber is a result of localized stress. The sources of this stress could be from ion implantation and sputtering of the phase and/or anisotropic thermal expansion coefficients within the phases. The hcp BN phase is then strained by the impingement and implantation of the xenon ions within its close-packed matrix. In HETs, accelerated ions have a range of energies between about 100 and 300 eV for a discharge voltage of 300 V [31]. In this work, we assume average ion impact energy of 110 eV to account for the fact that only the radial component of the ion velocity vector is perpendicular to the material surface. Furthermore, the plume plasma potential and the cathode coupling voltage reduce the effective potential drop experienced by the ions for acceleration for a given HET discharge voltage. Based on the Monte Carlo simulation "Stopping Range of Ions in Materials (SRIM)" [32], the average implantation depth at 110 eV into BN at normal incidence is approximately 2.0 nm with a straggle distance of 1.4 nm. In contrast, silica, being amorphous, would not have any crystallographic sputtering-dependent behavior and would also have more free volume because of its amorphous structure. This open structure could more easily accommodate localized strain created by the implantation of the ions. SRIM calculations show that the average implantation depth is 3.0 nm with a straggle distance of 2.2 nm for 110 eV xenon ions at normal incidence in silica. In either case, the implantation is a very near surface effect.

Though sputtering and implantation effects are possible mechanisms of creating cracks, the dominant mechanism is believed to be the anisotropic thermal expansion α of BN within the silica matrix. Because it is amorphous, silica will not have any anisotropic crystallographic thermal expansion behavior. Table 1 contains the elastic constants and Table 2 lists the thermal expansion coefficients for hBN. The thermal expansion coefficients were obtained from experiments conducted by Pease [33], which are in agreement with other values found in the literature [34,35]. Because the thermal expansion coefficient in the close-packed basal plane direction is not constant, a mean value was used in the models. That is,

$$\alpha_2 = \left(\int_0^{T_{\max}} \alpha_2^{\mathrm{ref}}(t) \, \mathrm{d}t \right) / T_{\max}$$

where $\alpha_2^{\mathrm{ref}}(t)$ is the temperature-dependent thermal expansion coefficient, and $T_{\max}$ is the final temperature of the model, which in this case is 800 K. This guarantees the correct thermal expansion at $T_{\max}$.

The silica phase was assumed to be isotropic with elastic constant $E = 70$ GPa[33] and thermal expansion coefficient $\alpha = 0.75 \times 10^{-6}/\mathrm{K}$ [36]. Using these values, the thermomechanical response within material was computed through a direct numerical simulation of the microstructure. The geometry of the microstructure was reconstructed using a finite element mesh created from a representative micrograph of the material, Figs. 6a and 6b. More specifically, the boundaries between the dark (BN) and light ($\mathrm{SiO_2}$) phases were drawn on top of the micrograph, as shown in Fig. 6a. Subsequently, a seed mesh size of 0.13 μm was specified along those boundaries. The entire region was then meshed using the prescribed boundary and seed constraints. The resulting mesh for the entire analysis domain is depicted in Fig. 6b. For the thermal expansion notation, the subscript for direction 1 denotes the normal to the basal plane, whereas directions 2 and 3 are within the basal plane and mutually orthogonal. From the previous TEM micrograph, Fig. 4, the basal plane was found to run parallel to the long axis of the hBN's fiber morphology. This crystallography–morphology relationship

Table 1 Elastic constants for BN [33][a]

Elastic constants, GPa	
C_{3333}	900
C_{2233}	200
C_{2323}	700
C_{1133}	2
C_{1111}	27
C_{1313}	5

[a]For the indices, direction 1 corresponds to the direction perpendicular to the basal plane, whereas directions 2 and 3 are within the basal plane.

Table 2 Thermal expansion coefficients for BN [36][a]

Thermal expansion, $10^{-6}/\mathrm{K}$	
α_1	40.5
α_2	−1.43
α_3	−1.43

[a]Direction 1 corresponds to the direction perpendicular to the basal plane. Values in the basal plane (directions 2 and 3) are mean values over the range of temperatures.
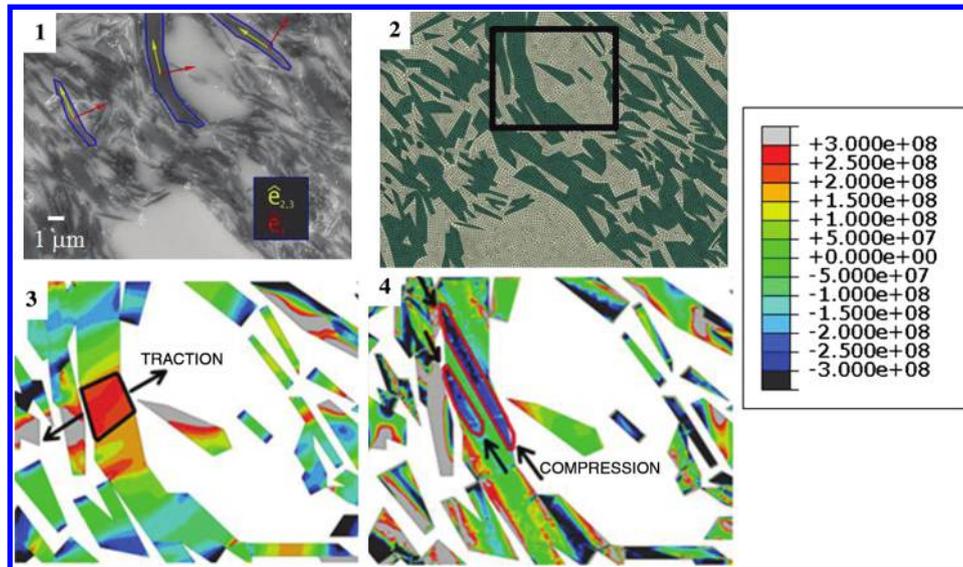
Fig. 6   a) SEM micrograph of the microstructure. b) Finite element simulated microstructure based on Fig. 6a. c) Stress component map perpendicular to the basal plane from region in Fig. 6b. d) Stress component map parallel to the basal plane from the region in Fig. 6b.

was used to estimate the approximate orientation of the hBN phase with this microstructure.

A uniform change in temperature of 500 K was applied and the thermal stresses determined for the free thermal expansion of the sample under plane strain conditions. The BN anisotropy leads to high stresses within the microstructure, evident by the stress gradients seen in Figs. 6c and 6d. Figure 6d shows the detail for a specific grain, taken from the box in Fig. 6b, in which the stress component perpendicular to the basal plane is purely tensile, with values reaching 200 MPa. For the same grain, Fig. 6e, compressive stresses are present in the in-plane direction. This particular stress state (i.e., tensile perpendicular to the basal plane and compressive within the plane) could initiate microcracking. Hexagonal close-packed BN has been previously shown to prevalently crack along the basal plane [37], which was also shown in this work. The thermal cycling values and conditions are significant and could lead to delamination cracking during the thermal loading. This cracking is evidence of the reaction of the material to anisotropic stress states while fixed within the microstructure. The detachment of surface BN grains is in response to these states upon thermal unloading, when the overall homogenized compressive stress is relieved. This is believed to be a dominant mechanism for the exfoliation of the hBN in the postanalyzed HE region.

In summary, we believe that the observed level of thermal stresses could lead to the formation of the observed microcracks. The formation of microcracks could favor a grain detachment process leading to ejection of hBN grains on the surface of the material. This process would, in turn, expose large silica areas to the sputtering effects of the plasma. Because silica has a higher sputtering rate than hBN, this mechanism could imply higher overall erosion rates for the compound, thus limiting the lifetime of HETs.

Conclusions

An HET wall, subjected to xenon plasma at power levels of 1.5–5 kW for approximately 2000 h, was characterized to determine the major features of erosion. Depending upon location in the chamber wall, the following three distinct regions were identified: 1) low erosion, 2) moderate erosion, and 3) high erosion. The LE region did not show any distinct erosion features. The ME region showed the onset of surface roughening in the form of surface striations and protrusions from line-of-sight sputter erosion. The onset of microcracking in the hBN was also observed. The HE region exhibited significant surface roughening, exfoliation of hBN from the surface and microcracking within the hBN. In addition, a darker discoloration was present on the surface of the HE region and

believed to be the result of carbon redeposition from the vacuum facility downstream graphite beam dump onto the HET. The major source of mechanical stress that contributed to the microcracking is the anisotropic thermal expansion of hBN in the silica matrix. As hBN thermally expanded in the more rigid silica matrix, in response to the high-temperature plasma, stress concentrations develop, resulting in microcracking parallel to the basal plane. In some instances, the surface hBN was liberated from the matrix material to accommodate this expansion, revealing a smooth silica surface. The prevalent microcracking in hBN is suggestive of weak structural integrity during plasma exposure for this particular heterogeneous ceramic composite. This work highlights the need for understanding how microstructure affects thermal stresses, microcracking, and sputtering, and how these factors may interact with each other to increase or decrease the effective erosion rate of a given material. Further knowledge in this area could prove useful for the selection of discharge channel materials in future HETs.

References

[1] Byers, D. C., "Geosynchronous-Earth-Orbit Communication Satellite Deliveries with Integrated Electric Propulsion," *Journal of Propulsion and Power*, Vol. 24, No. 6, 2008, pp. 1369–1375.
doi:10.2514/1.35322

[2] Brown, D. L., Beal, B. E., and Haas, J. M., "Air Force Research Laboratory High Power Electric Propulsion Technology Development," *IEEE Aerospace Conference*, Big Sky, MT, March 2010.

[3] Zhurin, V. V., Kaufman, H. R., and Robinson, R. S., "Physics of Closed Drift Thrusters," *Plasma Sources Science and Technology*, Vol. 8, No. 1, 1999, pp. R1–R20.
doi:10.1088/0963-0252/8/1/021

[4] Oh, D. Y., Randolph, T., and Kimbrel, S., "End-to-End Optimization of Chemical-Electric Orbit-Raising Mission," *Journal of Spacecraft and Rockets*, Vol. 41, No. 5, 2004, pp. 831–839.
doi:10.2514/1.13096

[5] Hofer, R. R., Mikellides, I. G., Katz, I., and Goebel, D. M., "BPT-4000 Hall Thruster Discharge Chamber Erosion Model Comparison with Qualification Life Test Data," *30th International Electric Propulsion Conference*, IEPC Paper 2007-267, Florence, Italy, 2007.

[6] de Grys, K., Mathers, A., Welander, B., and Khayms, V., "Demonstration of 10,400 Hours of Operation on a 4.5 kW Qualification

Model Hall Thruster," *46th AIAA/ASME/SAE/ASEE Joint Propulsion Conference and Exhibit*, AIAA Paper 2010-6698, 2010.

[7] Gascon, N., Dudeck, M., and Barral, S., "Wall Material Effects in Stationary Plasma Thrusters. I. Parametric Studies of an SPT-100," *Physics of Plasmas*, Vol. 10, No. 10, 2003, p. 4123.
doi:10.1063/1.1611880

[8] Barral, S., Makowski, K., Peradzyński, Z., Gascon, N., and Dudeck, M., "Wall Material Effects in Stationary Plasma Thrusters. II. Near-Wall and In-Wall Conductivity," *Physics of Plasmas*, Vol. 10, No. 10, 2003, p. 4137.
doi:10.1063/1.1611881

[9] Seiler, H., "Secondary Electron Emission in the Scanning Electron Microscope," *Journal of Applied Physics*, Vol. 54, No. 11, 1983, pp. R1–R18.
doi:10.1063/1.332840

[10] Mikellides, I., Katz, I., Hofer, R., and Goebel, D., "Design of a Laboratory Hall Thruster with Magnetically Shielded Channel Walls, Phase III: Comparison of Theory with Experiment," *48th AIAA Joint Propulsion Conference*, AIAA Paper 2012-3789, July 2012.

[11] Pellerin, N., Balika, L., Pellerin, S., Fosca, C., Véron, E., Pagon, D., and Dudeck, M., "Aging of Ceramics in a Hall Effect Plasma Thruster," *20th International Symposium on Plasma Chemistry 2011*, International Plasma Chemistry Society, Paper 20-66, 2011.

[12] Yalin, A. P., Rubin, B., Domingue, S. R., Glueckert, Z., and Williams, J. D., "Differential Sputter Yields of Boron Nitride, Quartz, and Kapton Due to Low Energy Xe+ Bombardment," *43rd AIAA/ASME/SAE/ASEE Joint Propulsion Conference*, AIAA Paper 2007-5314, 2007.

[13] Gamero-Castano, M., and Katz, I., "Estimation of Hall Thruster Erosion Using HPHall," *29th International Electric Propulsion Conference*, Electric Rocket Propulsion Society, Paper 05-303, 2005.

[14] Kim, V., Kozlov, V., Semenov, A., and Shkarban, I., "Investigation of the Boron Nitride Based Ceramics Sputtering Yield Under its Bombardment by Xe and Kr ions," *International Electric Propulsion Conference*, Electric Rocket Propulsion Society, Paper 01-073, 2001.

[15] Garnier, Y., Viel, V., Roussel, J.-F., Pagnon, D., Mange, L., and Touzeau, M., "Investigation of Xenon Ion Sputtering of One Ceramic Material Used in SPT Discharge Chamber," *International Electric Propulsion Conference*, Electric Rocket Propulsion Society, Paper 99-083, 1999.

[16] Garnier, Y., Viel, V., Roussel, J.-F., and Bernard, J., "Low-Energy Xenon Ion Sputtering of Ceramics Investigated for Stationary Plasma Thrusters," *Journal of Vacuum Science and Technology A: Vacuum, Surfaces, and Films*, Vol. 17, No. 6, 1999, pp. 3246–3254.
doi:10.1116/1.582050

[17] Zhang, J., Bhattacharjee, S., Shutthanandan, V., and Ray, P. K., "Sputtering Investigation of Boron Nitride with Secondary Ion and Secondary Neutral Mass Spectrometry," *Journal of Vacuum Science and Technology A: Vacuum, Surfaces, and Films*, Vol. 15, No. 2, 1997, pp. 243–247.
doi:10.1116/1.580519

[18] Mayrhofer, P. H., Mitterer, C., Hultman, L., and Clemens, H., "Microstructural Design of Hard Coatings," *Progress in Materials Science*, Vol. 51, No. 8, 2006, pp. 1032–1114.
doi:10.1016/j.pmatsci.2006.02.002

[19] Zidar, D. G., and Rovey, J. L., "Boron Nitride Hall-Effect Thruster Channel Surface Properties Investigation," *47th AIAA/ASME/SAE/ASEE Joint Propulsion Conference and Exhibit*, AIAA Paper 2011-5993, 2011.

[20] Haas, J. M., "Low-Perturbation Interrogation of the Internal and Near-Field Plasma Structure of a Hall Thruster Using a High-Speed Probe Positioning System," Ph.D. Dissertation, Univ. of Michigan, Ann Arbor, MI, 2001.

[21] Goebel, D. M., and Katz, I., *Fundamentals of Electric Propulsion: Ion and Hall Thrusters*, Vol. 1, Wiley, Hoboken, NJ, 2008, pp. 325–326.

[22] Haas, J. M., and Gallimore, A. D., "Internal Plasma Potential Profiles in a Laboratory-Model Hall Thruster," *Physics of Plasmas*, Vol. 8, No. 2,

2001, pp. 652–660.
doi:10.1063/1.1338535

[23] Alfred, L., Schwetz, K. A., and Hunold, K., "Hexagonal Boron Nitride: Fabrication, Properties and Applications," *Journal of the European Ceramic Society*, Vol. 5, No. 1, 1989, pp. 3–9.

[24] Mayer, J., Giannuzzi, L. A., Kamino, T., and Michael, J., "TEM Sample Preparation and FIB-Induced Damage," *MRS Bulletin*, Vol. 32, No. 5, 2007, pp. 400–407.
doi:10.1557/mrs2007.63

[25] Giannuzzi, L. A., "Reducing FIB Damage Using Low Energy Ions," *Microscopy and Microanalysis*, Vol. 12, No. S02, 2006, p. 1260.

[26] Wang, Z. L., "New Developments in Transmission Electron Microscopy for Nanotechnology," *Advanced Materials*, Vol. 15, No. 18, 2003, pp. 1497–1514.
doi:10.1002/adma.200300384

[27] Mazouffre, S., Echegut, P., and Dudeck, M., "Infrared Thermography Study on the Thermal Load Experienced by a High Power Hall Thruster," *International Electric Propulsion Conference*, Electric Rocket Propulsion Society, Paper 2005-063, 2005.

[28] Shastry, R., "Experimental Characterization of the Near-Wall Region in Hall Thrusters and Its Implications on Performance and Lifetime," Ph.D. Dissertation, Univ. of Michigan, Ann Arbor, MI, 2011.

[29] Drotar, J. T., Zhao, Y.-P., Lu, T.-M., and Wang, G.-C., "Surface Roughening in Shadowing Growth and Etching in 2 + 1 Dimensions," *Physical Review B: Solid State*, Vol. 62, No. 3, 2000, p. 2118.
doi:10.1103/PhysRevB.62.2118

[30] Meng, C., Rohrbach, C., Neuffer, A., Barth, K.-L., and Lunk, A., "Simulation of Boron Nitride Sputtering Process and Its Comparison with Experimental Data," *IEEE Transactions on Plasma Science*, Vol. 26, No. 6, 1998, pp. 1713–1717.
doi:10.1109/27.747890

[31] Gulczinski, F. S., "Examination of the Structure and Evolution of Ion Energy Properties of a 5 kW Class Laboratory Hall Effect Thruster at Various Operational Conditions," Ph.D. Thesis, Univ. of Michigan, Ann Arbor, MI, 1999.

[32] Ziegler, J. F., Ziegler, M. D., and Biersack, J. P., "SRIM–The Stopping, and Range of Ions in Matter (2010)," *Nuclear Instruments and Methods in Physics Research Section B: Beam Interactions with Materials and Atoms*, Vol. 268, No. 11, 2010, pp. 1818–1823.
doi:10.1016/j.nimb.2010.02.091

[33] Pease, R. S., "X-Ray Study of Boron Nitride," *Acta Crystallographica*, Vol. 5, No. 3, 1952, p. 356.
doi:10.1107/S0365110X52001064

[34] Hamdi, I., and Meskini, N., "Ab Initio Study of the Structural, Elastic, Vibrational and Thermodynamic Properties of the Hexagonal Boron Nitride: Performance of LDA and GGA," *Physica B: Physics of Condensed Matter*, Vol. 405, No. 13, 2010, pp. 2785–2794.
doi:10.1016/j.physb.2010.03.070

[35] Paszkowicz, W., Pelka, J. B., Knapp, M., Szyszko, T., and Podsiadlo, S., "Lattice Parameters and Anisotropic Thermal Expansion of Hexagonal Boron Nitride in the 10-297.5 K Temperature Range," *Applied Physics A: Materials Science and Processing*, Vol. 75, No. 3, 2002, pp. 431–435.
doi:10.1007/s003390100999

[36] Bauccio, M. (ed.), *ASM Engineered Materials Reference Book*, 2nd ed., ASM International, Materials Park, OH, 1994, p. 322.

[37] Trice, R. W., and Halloran, J. W., "Investigation of the Physical and Mechanical Properties of Hot-Pressed Boron Nitride/Oxide Ceramic Composites," *Journal of the American Ceramic Society*, Vol. 82, No. 9, 1999, pp. 2563–2565.
doi:10.1111/j.1151-2916.1999.tb02123.x

S. Son
Associate Editor